Quantifying the image quality and dose reduction of respiratory triggered 4D cone-beam computed tomography with patient-measured breathing

Benjamin J Cooper[1,2]**, Ricky T O'Brien**[1]**, John Kipritidis**[1]**, Chun-Chien Shieh**[1] **and Paul J Keall**[1]

[1] Radiation Physics Laboratory, Sydney Medical School, University of Sydney, NSW 2006, Australia
[2] Department of Medical Physics and Radiation Engineering, The Canberra Hospital, Canberra, ACT 2605, Australia

Corresponding Author Ben Cooper E-mail: ben.cooper@act.gov.au

Abstract

Respiratory triggered four dimensional cone-beam computed tomography (RT 4D CBCT) is a novel technique that uses a patient's respiratory signal to drive the image acquisition with the goal of imaging dose reduction without degrading image quality. This work investigates image quality and dose using patient-measured respiratory signals for RT 4D CBCT simulations. Studies were performed that simulate a 4D CBCT image acquisition using both the novel RT 4D CBCT technique and a conventional 4D CBCT technique. A set containing 111 free breathing lung cancer patient respiratory signal files was used to create 111 pairs of RT 4D CBCT and conventional 4D CBCT image sets from realistic simulations of a 4D CBCT system using a Rando phantom and the digital phantom, XCAT. Each of these image sets were compared to a ground truth dataset from which a mean absolute pixel difference (*MAPD*) metric was calculated to quantify the degradation of image quality. The number of projections used in each simulation was counted and was assumed as a surrogate for imaging dose. Based on 111 breathing traces, when comparing RT 4D CBCT with conventional 4D CBCT, the average image quality was reduced by 7.6% (Rando study) and 11.1% (XCAT study). However, the average imaging dose reduction was 53% based on needing fewer projections (617 on average) than conventional 4D CBCT (1320 projections). The simulation studies have demonstrated that the RT 4D CBCT method can potentially offer a 53% saving in imaging dose on average compared to conventional 4D CBCT in simulation studies using a wide range of patient-measured breathing traces with a minimal impact on image   qualit

1.   Introduction

Four dimensional cone beam computed tomography (4D CBCT) is growing as a tool for assessing organ and target motion due to respiration on the day of treatment. Numerous reports have been published on the use of 4D CBCT to evaluate and reduce setup error and to monitor the tumour trajectory (Sonke *et al* 2008, Qi and Chen 2011, Sweeney *et al* 2012, Takahashi *et al* 2013). Unfortunately, in general there are problems that hinder the practical implementation of 4D CBCT imaging into routine clinical treatment which several authors summarize as: (i) increased acquisition time; (ii) increased imaging dose; and (iii) uneven projection distributions leading to view-aliasing and streaking in the reconstruction images (Leng *et al* 2008b, Rosu and Hugo 2012, Fast *et al* 2013). Furthermore, Fast *et al* point out that making an improvement in one of these problems tends to come at the cost of degrading one of the others (Fast *et al* 2013).

There has been a good deal of research to try and improve on these problems and a variety of strategies have been pursued. Earlier work has shown that a slow-gantry technique can improve image quality (Li and Xing 2007, Lu *et al* 2007) and accordingly acquisition time lengthens. Leveraging improvements in computational power, especially exploiting the capability of GPUs, has led to the exploration and development of iterative based algorithms with the goal of obtaining high quality CBCT images from under-sampled and noisy projection data as a consequence of reducing applied imaging dose (Jia *et al* 2010, 2011). Streak free, high temporal resolution image volumes from vastly undersampled cone-beam projections in conjunction with a fully sampled prior image have been reported using a custom PICCS algorithm (Leng *et al* 2008a). Ahmad *et al* showed that the most influential object parameter for 4D-CBCT performance is the period of motion of the object and published recommendations for minimum scan times according to object size and period of motion (Ahmad and Pan 2012). Brehm *et al* propose a motion-compensated reconstruction technique that does not use a prior planning CT image but instead applies a deformation based on estimated motion vector fields from all respiratory phases from the same imaging session thus removing any influence of anatomical changes between planning and treatment (Brehm *et al* 2011). Frustratingly, the problem of building a motion model from CBCT projection data is ill-posed (Rit *et al* 2009) as the motion models are generally sensitive to streak artifacts from undersampling. To help address this, Brehm *et al* model a patient specific undersampling artifact and then use this information to compensate for its effects on the motion vector field leading to imaging volumes of high quality (Brehm *et al* 2013). Zhang *et al* simulated a lung patient with anatomical changes between planning 4D-CT to onboard imaging. The prior 4D-CT scans were used in conjunction with limited angle onboard cone-beam projections to develop a motion modelled free-form deformation technique leading to improved accuracy in estimating target volume and centre of mass changes (Zhang *et al* 2013). Wang and Gu used the projections collected from on-treatment CBCT in a 'warm start', two step optimization process that deforms the planning CT without the need for a prior motion model of the patient, aiming to produce high quality 4D-CBCT (Wang and Gu 2013).

Another approach to improving 4D CBCT involves incorporating a breathing signal as a feedback into the control systems responsible for acquiring projections. Fast *et al* demonstrated an experimental 4D CBCT acquisition technique that takes a breathing signal, either external motion sensor or electromagnetic transponder based, and actively triggers desirable projections to efficiently utilize dose and eliminate

motion blurring from sinusoidal trajectories in anthropomorphic lung phantom studies (Fast *et al* 2013). Kincaid *et al* have developed a gated CBCT technique that focusses on acquiring narrowly spaced projections for up to a 30% 'on' gated window using a programmed gantry motion that 'rewinds' the gantry position to continue acquisition where it left off at the end of the last 'on' gated window (Kincaid Jr *et al* 2013). O'Brien *et al* presented an optimization algorithm that responds to a respiratory signal with the aim of obtaining evenly spaced projections for all respiratory bins by allowing a constrained variation on gantry velocity and variation on projection frequency (O'Brien *et al* 2013, 2014).

In this space, we introduced a method, 'Respiratory Triggered' 4D CBCT (RT 4D CBCT). In RT 4D CBCT, a single projection is triggered once per respiratory bin per breathing period. Using this method, imaging dose can be reduced and image quality maintained using synthetic, regular sinusoidal breathing signals (Cooper *et al* 2013). The effects of breathing irregularities can impact on the performance of 4D CBCT (Lu *et al* 2007). This is why we make the crucial step towards clinical implementation of RT 4D CBCT in this work by investigating RT 4D CBCT's performance using real patient-measured breathing traces with the accompanying irregularities and unpredictable behaviour of the breathing signals. We compare image quality and estimated imaging dose using the RT 4D CBCT acquisition method and a conventional 4D CBCT acquisition method using the same patient-measured breathing trace in each case.

2.   Methods

2.1.   *Theory of RT 4D CBCT and conventional 4D CBCT simulations*

A brief explanation for RT 4D CBCT and its main difference from conventional 4D CBCT is presented for completeness but a detailed description of the RT 4D CBCT method can be found in a previously reported study with sinusoidal motion (Cooper *et al* 2013).

Trajectories for a kV source during an RT 4D CBCT (A) and a conventional (B) acquisition session are represented (figure 1). Just the projections collected for phase-bin 1 are shown.
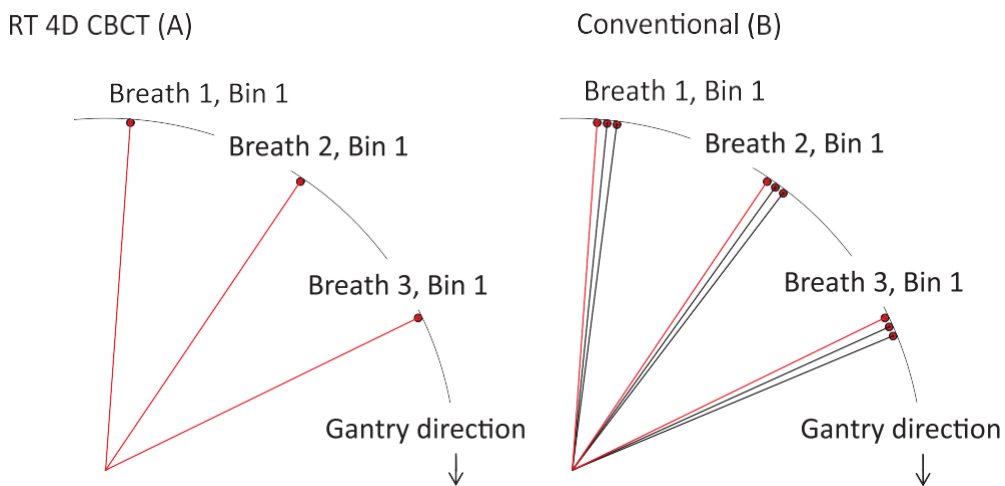

Figure 1. Projection schedule, phase-bin 1 for RT 4D CBCT (A) and conventional 4D CBCT (B).

We see the central idea of RT 4D CBCT (figure 1(A)) is that only one projection is allowed to be triggered per phase bin per breath. In contrast, during a conventional 4D CBCT acquisition (figure 1(B)) the projections are triggered at a constant rate with no feedback from the patient's respiratory signal resulting in tightly grouped clusters of projections.

There are two arms to this study: the RT 4D CBCT arm and the conventional 4D CBCT arm. The work flow for the simulation experiments in this study is illustrated (figure 2). The overview here is expanded upon in the following sections. In the current study, each of 111 lung cancer patient breathing traces are used to drive 111 pairs of separate simulations of an image acquisition session using the RT 4D CBCT method (figure 2, left) and another image acquisition session using the conventional 4D CBCT method (figure 2, right). Each simulation set of projection images is sent to a commercial FDK (Feldkamp *et al* 1984) reconstructor program, Cobra. The resulting images from each method are compared against a ground truth dataset from which the mean absolute pixel difference error (*MAPD*) and the imaging doses are reported.
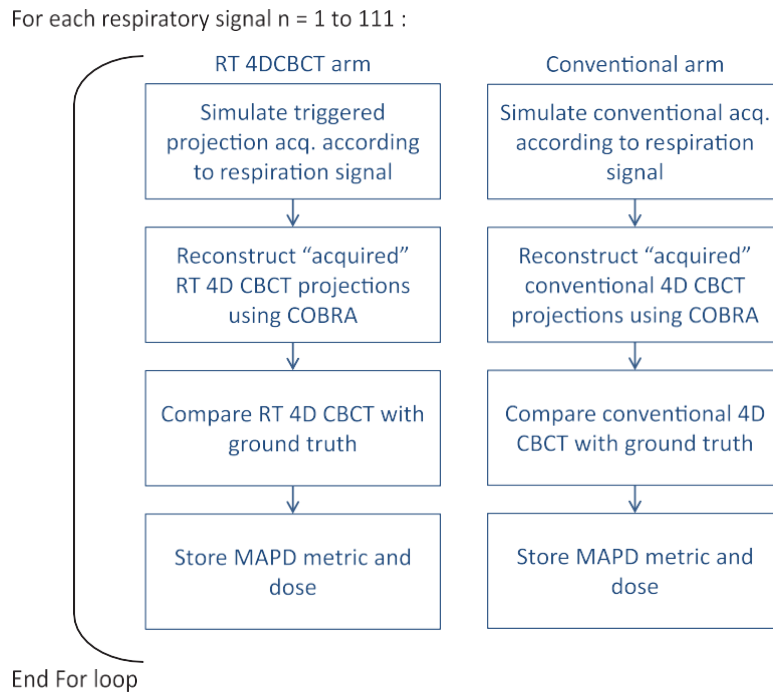
For each respiratory signal n = 1 to 111 :

RT 4DCBCT arm	Conventional arm
Simulate triggered projection acq. according to respiration signal	Simulate conventional acq. according to respiration signal
Reconstruct "acquired" RT 4D CBCT projections using COBRA	Reconstruct "acquired" conventional 4D CBCT projections using COBRA
Compare RT 4D CBCT with ground truth	Compare conventional 4D CBCT with ground truth
Store MAPD metric and dose	Store MAPD metric and dose

End For loop

Figure 2. Flow chart of the RT 4D CBCT and conventional 4D CBCT simulation arms.

2.2 Patient-measured breathing data

Breathing data in the form of external marker position data from 111 RPM files from 24 lung cancer patients measured under free breathing conditions in a previous study were utilized (George *et al* 2006). The data were used as an input driver for the RT 4D CBCT algorithm and used to break down the conventional 4D CBCT acquisition into 10 bins in the simulation experiments (figure 2).

2.3 RT 4D CBCT and conventional simulation software

The first box (figure 2, top, left), is expanded upon here to describe how the RT 4D CBCT module works. Simulation software has been built in-house which allows the study and simulation of 4D CBCT imaging techniques. This software platform was built for flexibility to allow different software implementations of image acquisition optimization modules. This allows the experimenter to enable or disable various combinations of algorithms for a given set of simulations. The RT 4D CBCT software module was built to accept a respiratory signal, specifically RPM data (version 1.4) as an input data stream. The studies use the recorded *. dat RPM files which contain the real-time phase estimates, not the *.vxp files which have phase re-calculated. The *.dat files represent phase estimations that are commercially achievable in a real-time system. The data is formatted as a comma separated list with the first three positions in a single line being: (i) detected displacement of marker block; (ii) respiratory phase (range 0–2π); (iii) time stamp. The marker block is an external surrogate for tumour motion which can lead to small time shifts and

amplitude mismatches; however, Ionascu *et al* have shown that the superior-inferior internal-external motion is well correlated in a small 10 patient study (Ionascu *et al* 2007). Numerous other works have investigated the correlation between tumour/organ motion and various surrogates (table 3, Keall *et al* (2006). Never the less, it is expected that there will be some patients amongst the cohort of 111 where marker correlation is poor potentially degrading image quality. The RT 4D CBCT algorithm takes an incoming respiratory signal and triggers based on the conditions outlined (figure 3). The RPM data is 'read in' in close to real-time to model as closely as possible the data stream that would be present in a real world clinical situation. As the respiratory signal data frames arrive (approximately every 33 ms), the software determines to which phase-bin the current signal frame belongs (b_{now}, figure 3) by reading the respiratory phase from the data frame. If b_{now} has changed from the previous signal frame, and we do not already have a projection in this bin for this breath, we trigger a projection, otherwise wait for the next signal frame. This continues until the end of the simulation run for this breathing trace. This is now repeated for each of 111 breathing traces (the outer loop, figure 2). One purpose for using the phase data directly 'as-is' from the RPM data stream without any post processing is for simplicity of implementation with the RPM system in widespread clinical use. Abdelnour *et al* describe some of the behaviours and limitations of the RPM system in detail (Abdelnour *et al* 2007).

The conventional 4D CBCT simulation runs (figure 2, right) are simulated using the same software platform but with the RT 4D CBCT module switched off. Referring to figure 3, switching off the RT 4D CBCT module is equivalent to skipping the numbered sections 2–4. The respiratory signal is now simply used to divide the projections into respiratory phase-bins for each of the 111 breathing traces.
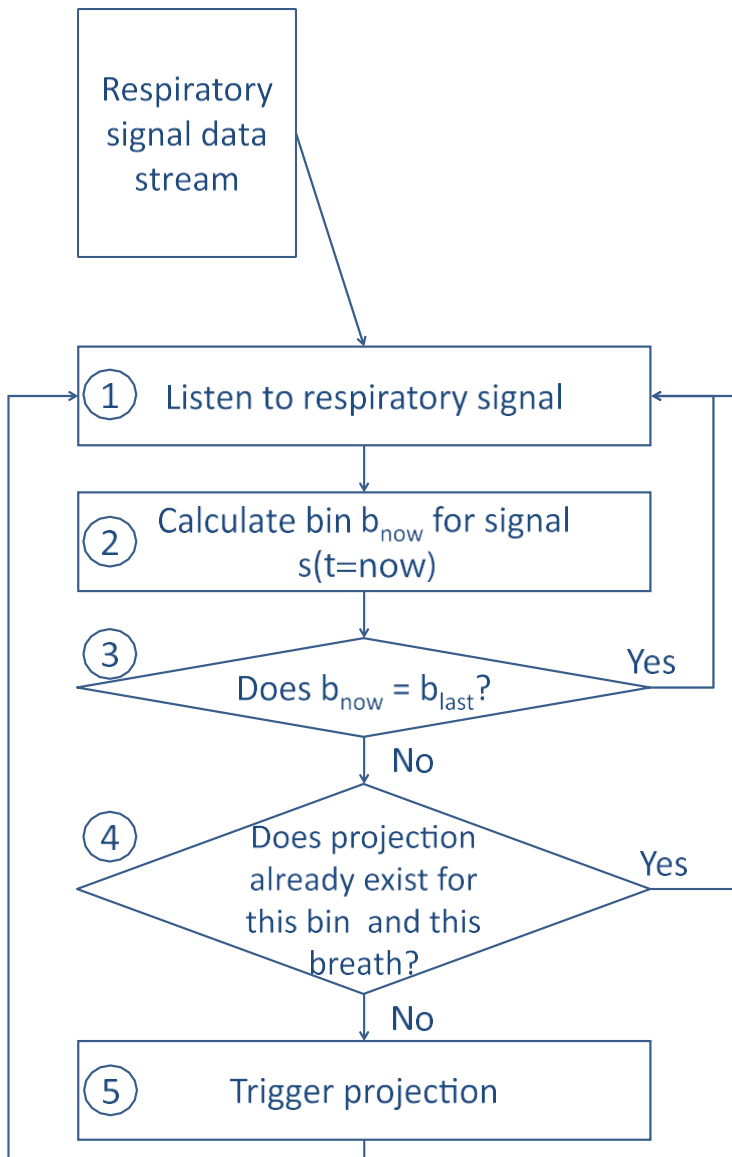
Figure 3. Algorithm controlling projection acquisition for RT 4D CBCT.

2.4   Experiments: ground truth, RT 4D CBCT and conventional acquisition simulations with RANDO phantom

Rando phantom studies were carried out to investigate the behaviour of the RT 4D CBCT acquisition technique driven by an irregular breathing signal. The benefit in using the static Rando phantom is that the effect of the irregular breathing signal on the projection triggering can be determined in isolation from the confounding effects of a moving tumour on image quality. See Shrimpton *et al* (1981) for details regarding the tissue equivalence of the Rando phantom for kilovoltage x-rays.

2.4.1   *Ground truth data.* A CBCT projection dataset from the thorax region of a static Rando phantom was collected using a very fine angular spacing (0.056°). This is the ground truth image dataset. It contains roughly 3600 projections over a 200 degree gantry sweep.

2.4.2   *RT 4D CBCT and conventional 4D CBCT simulations.* The RT 4D CBCT and conven- tional 4D CBCT simulations are 'synthetic' as they select projections according to the input respiratory signal from the static projections collected in section 2.4.1. All conventional 4D CBCT simulations are based on the acquisition parameters used from a commercially available 4D CBCT system as listed by Giaddui *et al* (2013):

- 200° span of gantry sweep;

- 240 s acquisition time;

- Imaging frequency of 5.5 Hz.

For the RT 4D CBCT simulations, only the imaging frequency is varied in accordance with the input respiratory signals; the acquisition time and gantry speed are the same as for the conventional simulations. For each simulation we collect data for the following properties: (i) how many projections were used; (ii) the angle of each projection (range: 0–200°); (iii) the respiratory bin of each projection (range: 1–10). For each of the simulated projections we find the closest matching 'real' projection from the Rando CBCT projection set (section 2.4.1) based on the simulation projection angles, and send those projections via a batch file to the Cobra CBCT reconstruction platform to reconstruct the simulation CBCT images.

2.5   Experiments: RT 4D CBCT and conventional acquisition simulations with XCAT phantom

The behaviour of the RT 4D CBCT acquisition technique and effect on image quality in the presence of irregular breathing and tumour motion was investigated using the XCAT digital phantom.

2.5.1   *XCAT phantom set up.* The XCAT digital phantom (Segars *et al* 2010) was configured to model a breathing patient. Existing RPM breathing signal data files were used as a data source for a representative spherical tumour motion and diaphragm motion within the capabilities of the XCAT tool kit.

The XCAT studies are included to determine the performance of the RT 4D CBCT method under conditions that attempt to represent a breathing patient *in silico*. The XCAT phantom has been used in these experiments to investigate these effects on image quality for both RT 4D CBCT and conventional 4D CBCT. It is necessary to use the XCAT phantom to understand the variations in tumour motion that comes from breathing patients.

During the course of a clinical 4D CBCT acquisition, projections are acquired as the patient breathes and the RPM system records displacement of the marker block. As a model for breathing, the displacement parameter from the RPM signal has been translated and normalized into a thoracic 'breathing' motion with a 2 cm superior-inferior range and 0.5 cm anterior-posterior range using the XCAT software. The minimum and maximum RPM displacement signal has been re-scaled to 0 cm and 2 cm tumour displacement respectively giving a 2 cm superior-inferior tumour excursion which is synchronised with the diphragm motion.

To illustrate this, the marker block displacement is plotted (figure 4). The dots represent where projections are acquired for a selected mid-inhale phase. The spread of dots is reflective of the difficulties in calculating real-time phase which leads to intermittent assignment of the gating phase interval to an incorrect portion of the respiratory trace (Santoro *et al* 2009). The simulations incorporate these difficulties associated with real-time phase calculation and the accompanying inconsistencies of tumour motion by directly using the real-time RPM data. We have used the real-time phase signal from the RPM system because it is in current use for clinical gating systems. The real-time phase from the RPM system is known to contain significant errors (Santoro *et al* 2009); however, the work of Ruan *et al* (2009) on real-time phase calculation methods demonstrate improvements that would help address these issues.
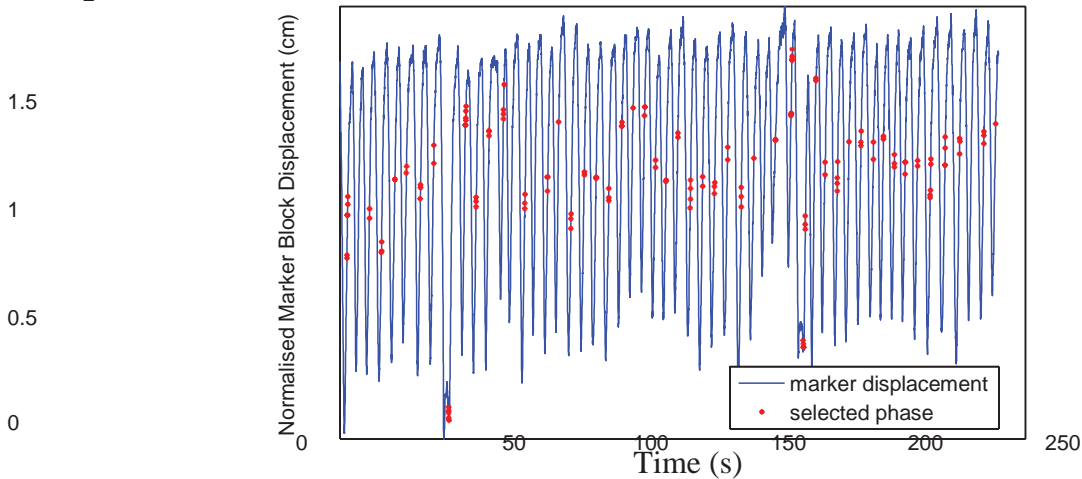
Figure 4. RPM marker displacement with dots representing where projections are taken for a selected mid-inhale phase.

A set of 50 'snapshot' 3D XCAT digital phantoms with the moving tumour embedded was created. If end-exhale is snapshot 1 with tumour displacement = 0.0 cm and end-inhale is snapshot 50 with tumour displacment = 2.0 cm, then each of the 50 snapshots steps up the tumour in 0.4 mm gradations from end-exhale to end-inhale giving a finely spaced set of tumour positions in the XCAT phantoms to sample the tumour motion. The normalized displacement values from each of the 111 breathing traces were used to select the appropriate XCAT 'snapshot' from the set of 50 XCAT phantoms thus giving the modelled instantaneous diaphragm and tumour position. The resulting series of XCAT snapshots effectively provide a model of diaphragm and tumour motion for a given RPM file. The 'ground truth' image for the XCAT simulations is taken to be the tumour in the middle of its trajectory between inhale and exhale and is taken from the middle of the range of the set of 50 XCAT phantoms. It is a deliberate choice not to include intra-phase blur in the XCAT ground truth to try and highlight the expected intra-phase blur resulting from both the conventional and RT 4D CBCT simulations.

RT 4D CBCT and conventional 4D CBCT XCAT simulations. A forward projection of each snapshot XCAT phantom for a given phase bin was generated to simulate the collection of an on-board imaging system projection frame using the RTK software suite (Rit *et al* 2014). Consider a single x-ray beamlet from the kV source: an upper limit intensity value is set to 65 535 ($2^{16} - 1$) representing no attenuation at all. As the beamlet passes through the XCAT phantom, the linear attenuation is determined and the resulting intensity value is registered as a pixel on the projection image. Image noise is modelled as Poisson noise via the Matlab function *imnoise*. In this manner, a complete set of x-ray projections is collected simulating the acquisition that occurs during a 4D CBCT imaging session of a breathing patient. Photon scatter from the kV source traversing through the phantom has not been considered. In an effort to capture the time snap, or phase-bin where the image reconstructions are likely to be the blurriest due to maximal instantaneous tumour motion, the phase-bin that sits half way between inhale and exhale was chosen for projection collection. These projections were then fed in to the Cobra reconstruction engine to produce the CBCT image reconstructions.

2.5.2 *RT 4D CBCT and equivalent dose conventional 4D CBCT XCAT simulations.* The conventional 4D CBCT simulations were repeated but using the same number of projections as the corresponding RT 4D CBCT simulations. This is referred to as *equivalent dose conventional 4D CBCT* (EqD Conventional). These simulations could only be run retrospectively once the number of projections (imaging dose) was known for each of the 111 RT 4D CBCT simulations. Then for a given simulation, the EqD Conventional fixed triggering frequency is calculated by:

$$Triggering\ Frequency = \frac{N_{proj}}{240} \tag{1}$$

Triggering Frequency is given in Hz where N_{proj} is the number of projections from the RT 4D CBCT simulation and 240 is the number of seconds for the acquisition.

2.6. Image metrics: mean absolute pixel difference from ground truth (MAPD), image gradient and dose

All images were reconstructed using Cobra which outputs CT images with default, un-calibrated Hounsfield Unit (HU) gray scale, referred to as raw pixel gray level in this study. The mean absolute pixel difference (*MAPD*) is defined as the mean scalar pixel value difference between the ground truth CT image dataset and the RT 4D CBCT or conventional reconstructed CT image dataset. It is defined as follows:

$$MAPD = \frac{\sum_{i=1}^{N}|GT_i - X_i|}{N} \tag{2}$$

where N is the total number of pixels in a CT dataset, GT_i is the intensity of pixel i in a ground truth image dataset and X_i is the intensity of pixel i from either an RT 4D CBCT or conventional 4D CBCT reconstructed image dataset. Henceforth, *MAPD* always means the mean absolute pixel difference as defined here and it is always with respect to the ground truth CBCT image dataset. It has units of raw pixel gray level.

For the XCAT simulations, the change in pixel value in the superior-inferior (*y*) direction in a vertical line through the centre of the spherical tumour on a coronal image (*f*) was calculated. We define this as the superior-inferior image gradient and represent it simply as *SupInf*:

$$SupInf = \frac{\partial f}{\partial y} \tag{3}$$

The *SupInf* image gradient metric is chosen to focus on the tumour motion induced blurring of the image reconstructions. It is interpreted to describe the image sharpness of the tumour in the direction of the tumour motion. A sharper image of the tumour corresponds to a well defined peak-and-trough in the image gradient plot as is expected in a ground truth image with no tumour motion; a less sharp image will have a less well defined peak-and-trough gradient plot.

The total number of projections was counted for each simulation and it is assumed that one projection equals one arbitrary unit of imaging dose. As an indication of dose, Kim *et al* (2010) report that a low dose thorax imaging CBCT protocol with 677 projections gave a measured dose of 7.68 mGy.
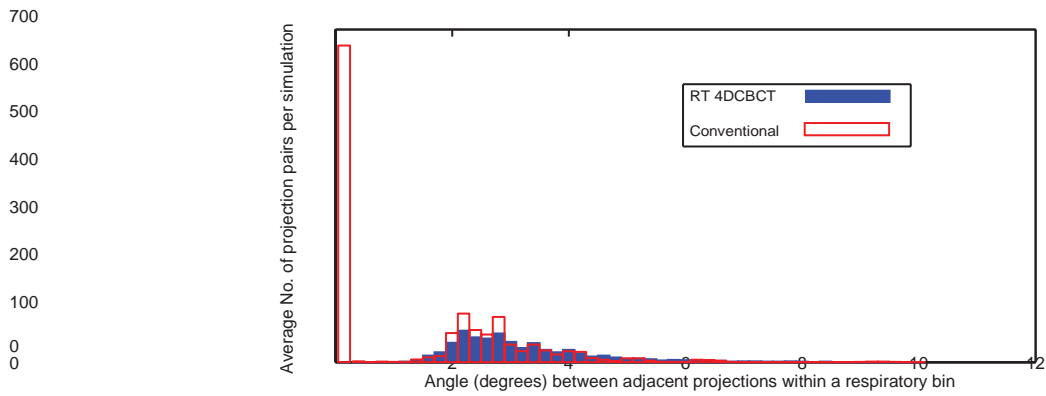
Figure 5. Angular distribution of adjacent projections for all bins over all paired 111 RT 4D CBCT and conventional simulations.

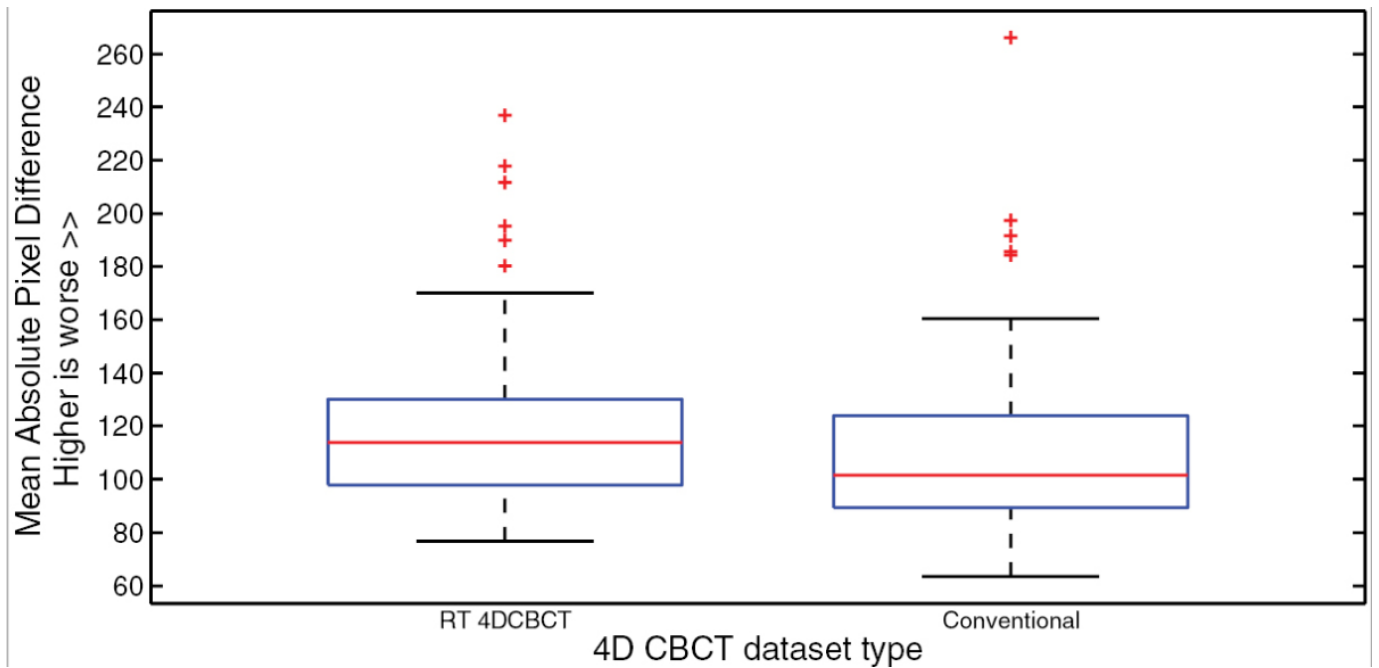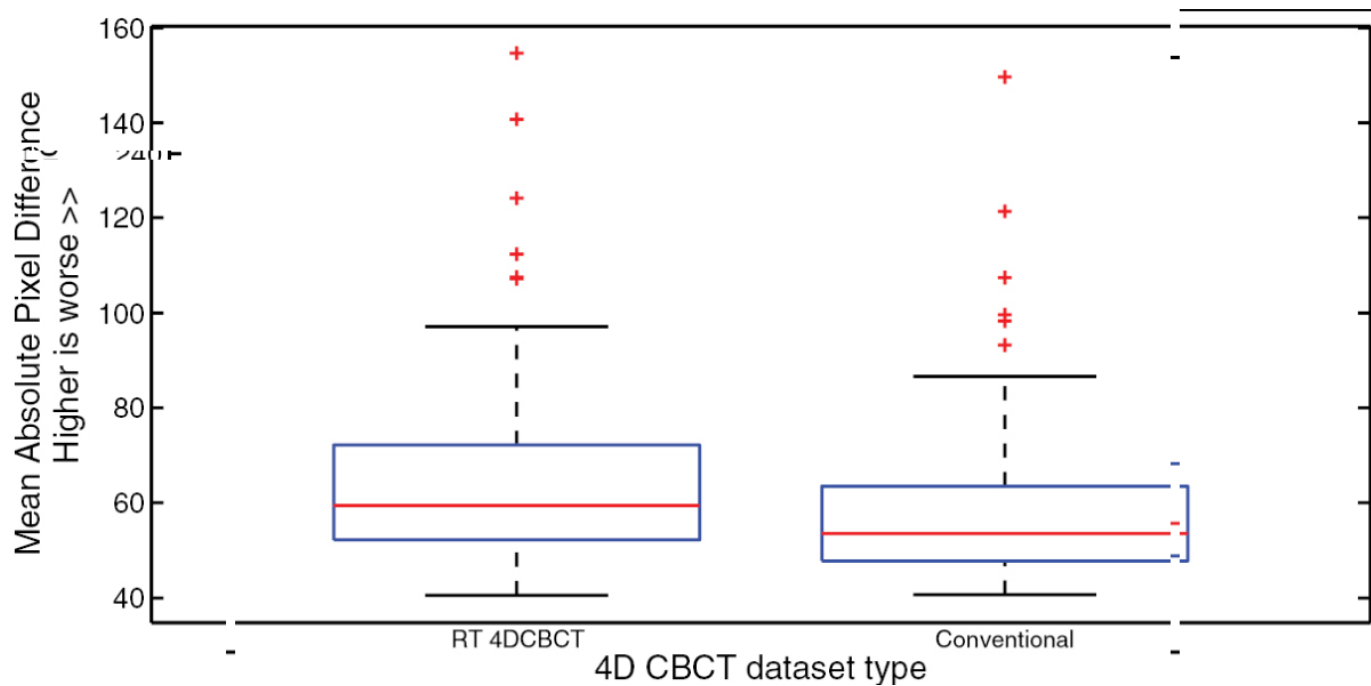**Figure 6.** Comparison of RT 4D CBCT and conventional image quality (*MAPD* from ground truth) for Rando   studies.

Figure 7. Comparison of RT 4DCBCT and conventional image quality (*MAPD* from ground truth) for XCAT studies.

3 Results

3.1 Angular separation of adjacent projections: distributions for RT 4D CBCT and conventional 4D CBCT

The distributions of angular separation between adjacent projections for all bins and all 111 breathing traces are shown for RT 4D CBCT and conventional 4D CBCT simulations (figure 5). The static Rando thorax phantom data is used here to study the effects on projection angular distribution and image quality from irregular breathing traces without the confounding effect of tumour motion. The striking feature of the conventional distribution is that it shows a large peak of adjacent projections in the first histogram bin with a small angular spacing. It represents projection 'doubling up' whereby two projections are acquired in the same bin with only a very small angular spacing ($\leq 0.2°$). In this scenario, the second projection within that bin is redundant and gives rise to extra imaging dose without much benefit. In contrast, the RT 4D CBCT method ensures that this doubling up of projections is avoided.

3.2 Mean absolute pixel difference from reference ground truth (MAPD)

The distributions of the *MAPD* for the RT 4D CBCT and conventional simulations from the 111 breathing traces are represented with boxplots for the Rando phantom data (figure 6) and the XCAT phantom data (figure 7).

The median values of the *MAPD* in units of raw pixel gray level value for RT 4D CBCT and conventional are 113.9 and 101.5 (Rando studies), 59.2 and 53.5 (XCAT studies) respectively; the corresponding mean values of *MAPD* are 119.2 and 110.8 (Rando studies), 65.1 and 58.6 (XCAT studies). Wilcoxon signed rank tests on the RT 4D CBCT and conventional *MAPD* distributions from the Rando and XCAT studies give a *p*-value $p < 0.001$ for both meaning that there are significant differences in the median values from the RT 4D CBCT and conventional datasets. Although statistically significant, the mean *MAPD* for RT 4D CBCT is only 7.6% worse than conventional for the Rando studies and 11.1% worse than conventional for the XCAT studies, taking conventional as the reference in both cases.

3.3 Image quality (MAPD from ground truth) versus dose

The image quality (*MAPD* from ground truth) versus imaging dose (or number of projections) for the 111 breathing traces used in the Rando and XCAT simulation studies are plotted respectively (figures 8–10). The open circles and squares represent the RT 4D CBCT and conventional acquisition methods respectively. For the RT 4D CBCT dataset, the number of projections (imaging dose) corresponding to the 25th, 50th and 75th percentile of *MAPD* are 486, 616, and 761 for the Rando studies (figure 8) and 492, 620, 770 for the XCAT studies (figure 9) respectively. The conventional simulations give an imaging dose that is fixed at 1320 projections for both the Rando and XCAT studies (figures 8 and 9). The equivalent dose conventional simulations have the same dose as the RT 4D CBCT simulations, by design (figure 10).

There are clear savings in imaging dose using the RT 4D CBCT method with only a 7.6% and 11.1%

reduction in image quality on average for the Rando and XCAT studies respectively (figures 8 and 9). Interestingly, when conventional XCAT simulations are repeated and 'clamped' to the same dose as the RT 4D CBCT simulations, the relationship between imaging quality and imaging dose takes on the same $1/x$ like shape as that for RT 4D CBCT (figure 10). Curve fitting was performed using a Matlab *power2* curve fitting model[7]. R-square values for RT 4D CBCT and EqD Conventional are 0.964 and 0.627 respectively, indicating a greater spread for the EqD Conventional data.

To try and visualize what a 7.6% reduction in image quality means qualitatively, CBCT reconstructions for RT 4D CBCT and conventional are shown (figure 11, top and bottom row respectively). Left to right shows representative images from the 25th, 50th, and 75th percentile of *MAPD*. It is apparent that there is very little difference comparing the top row (RT 4D CBCT) to the bottom row (conventional).
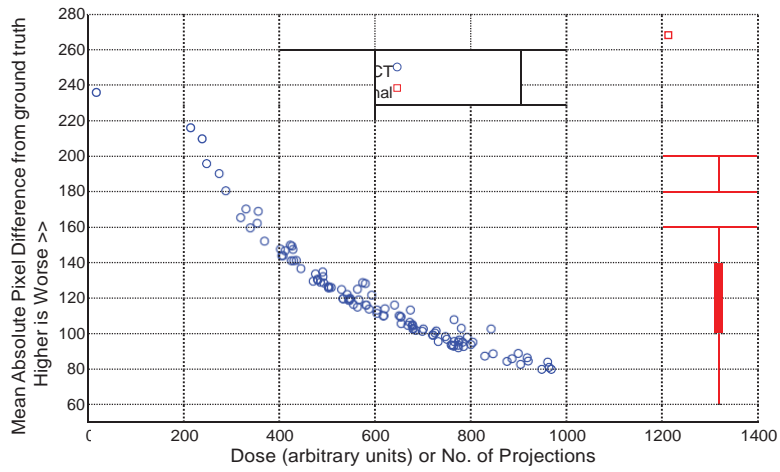
Figure 8. Image quality (*MAPD*) versus dose for RT 4D CBCT and conventional for Rando studies.
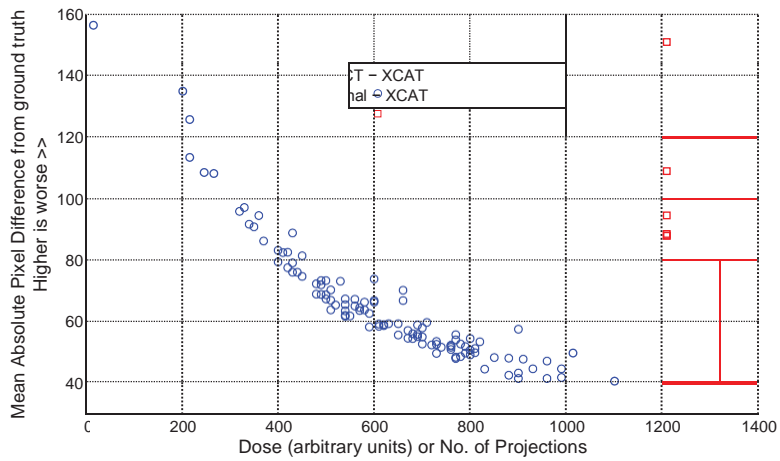

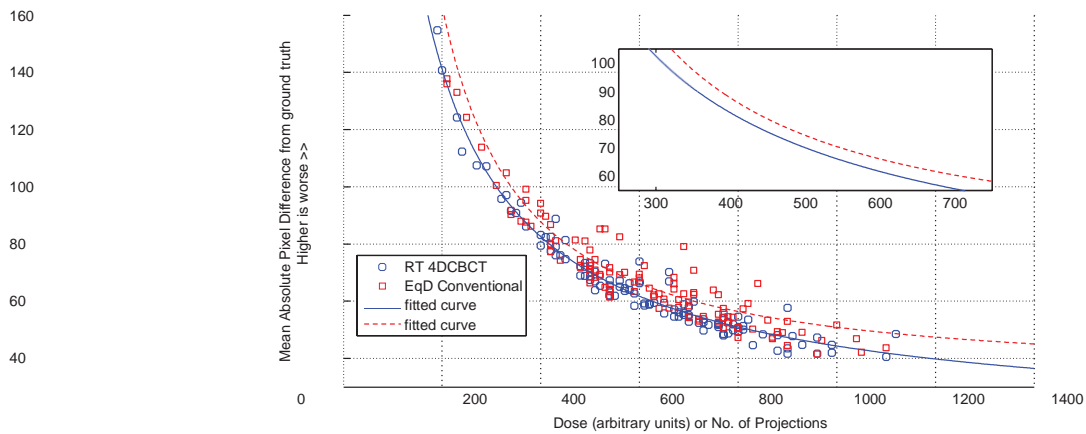**Figure 9.** Image quality (*MAPD*) versus dose for RT 4D CBCT and conventional for XCAT studies.

Figure 10. Image quality (*MAPD*) versus dose for RT 4D CBCT and EqD conventional for XCAT studies. The EqD conventional simulations use equivalent dose to RT 4D CBCT. Inset: fitted curves for RT 4D CBCT (solid) and EqD conventional (dashed) simulations shown without data tick marks for clarity.
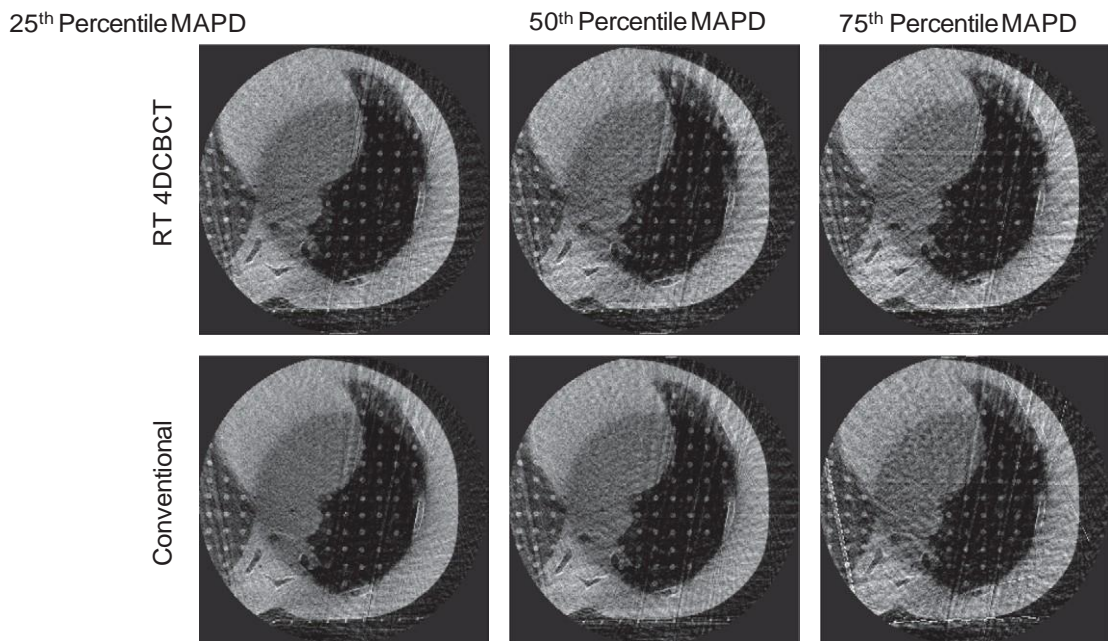

Figure 11. RT 4D CBCT (top row) and conventional (bottom row) showing images from the 25th, 50th, and 75th percentile of mean absolute pixel difference (*MAPD* from ground truth) between the reconstructed image and the ground truth.

3.4 Representative coronal reconstructions from XCAT phantom simulations

A subset of XCAT phantoms studies representing the 25th, 50th, and 75th percentile of *MAPD* from ground truth gives a visualization of the image quality and spatial resolve of the tumour. Single coronal image slices through the moving tumour from the RT 4D CBCT and conventional simulations and each of the 25th, 50th, and 75th percentile *MAPD* distributions are shown (figures 12–14). The 'ground truth' image in the XCAT simulations is the tumour in the middle of its trajectory between inhale and exhale (described in section 2.5.1). The respiratory bin 'capturing' the tumour midway through its trajectory is shown for simulations using RT 4D CBCT and conventional acquisition methods (figures 12–14, top and bottom rows, respectively). Using equation (2) the defined *MAPD* for the displayed coronal slice is calculated for RT 4D CBCT and conventional reconstruction techniques denoted as 'Av = ...' in the figures. The number of required projections are reported for each simulation and is denoted as 'n' (figures 12–14).

The vertical line over the tumour in figure 15 represents the pixels along which the previously defined *SupInf* image gradient is calculated (see equation (3)). figures 16–18 show the resulting calculations for the *SupInf* image gradient: the thick solid black line is the gradient for the ground truth and is repeated in each plot for reference. The dashed lines represent the gradient for RT 4D CBCT and the dotted lines represent the gradient for conventional simulations.
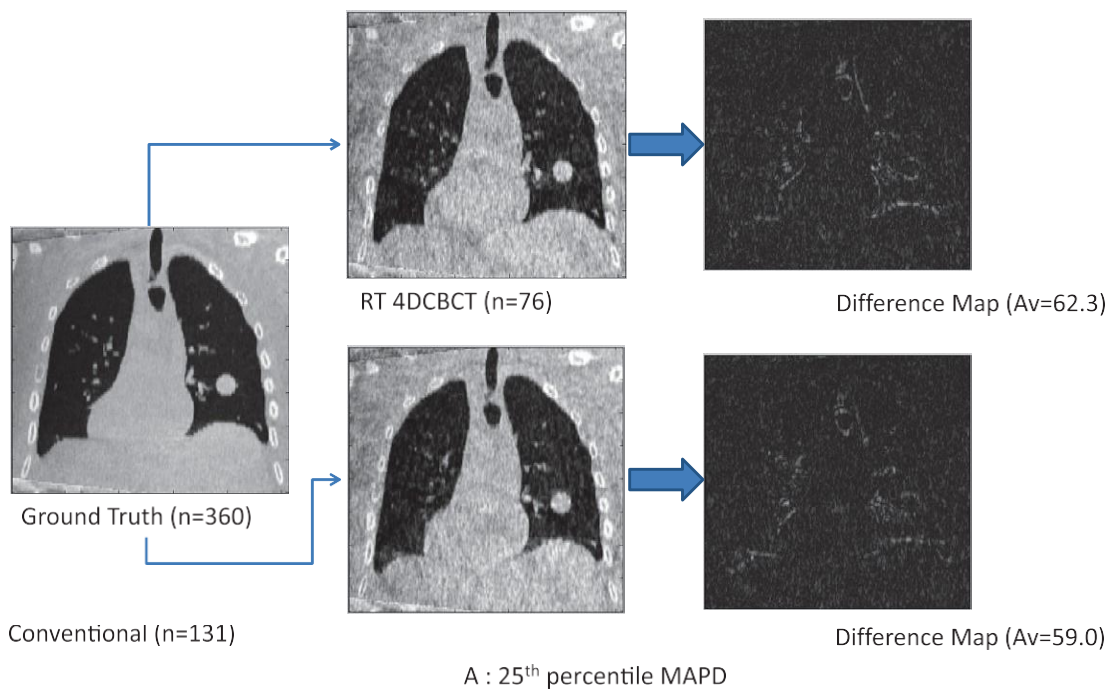
RT 4DCBCT (n=76)

Difference Map (Av=62.3)

Ground Truth (n=360)

Conventional (n=131)

Difference Map (Av=59.0)

A : 25th percentile MAPD

Figure 12. Coronal slices from XCAT simulation corresponding to 25th percentile of *MAPD*. Ground truth image (left), RT 4D CBCT (top) and conventional (bottom), difference maps (right). 'n' is number of projections required, 'Av' is average pixel difference from ground truth image.

RT 4DCBCT (n=73)

Ground Truth (n=360)

Conventional (n=131)

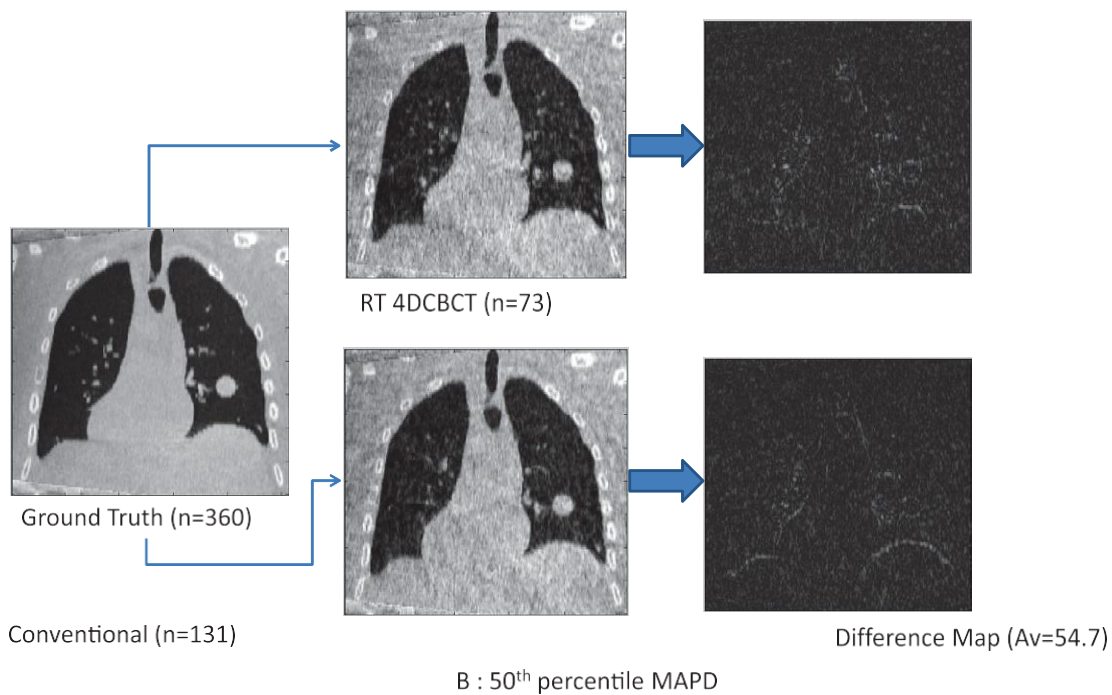Difference Map (Av=54.7)

B : 50th percentile MAPD

Figure 13. Coronal slices from XCAT simulation corresponding to 50th percentile of *MAPD*. Ground truth image (left), RT 4D CBCT (top) and conventional (bottom), difference maps (right). 'n' is number of projections required, 'Av' is average pixel difference from ground truth image.

RT 4DCBCT (n=49)   Difference Map (Av=83.0)

Ground Truth (n=360)

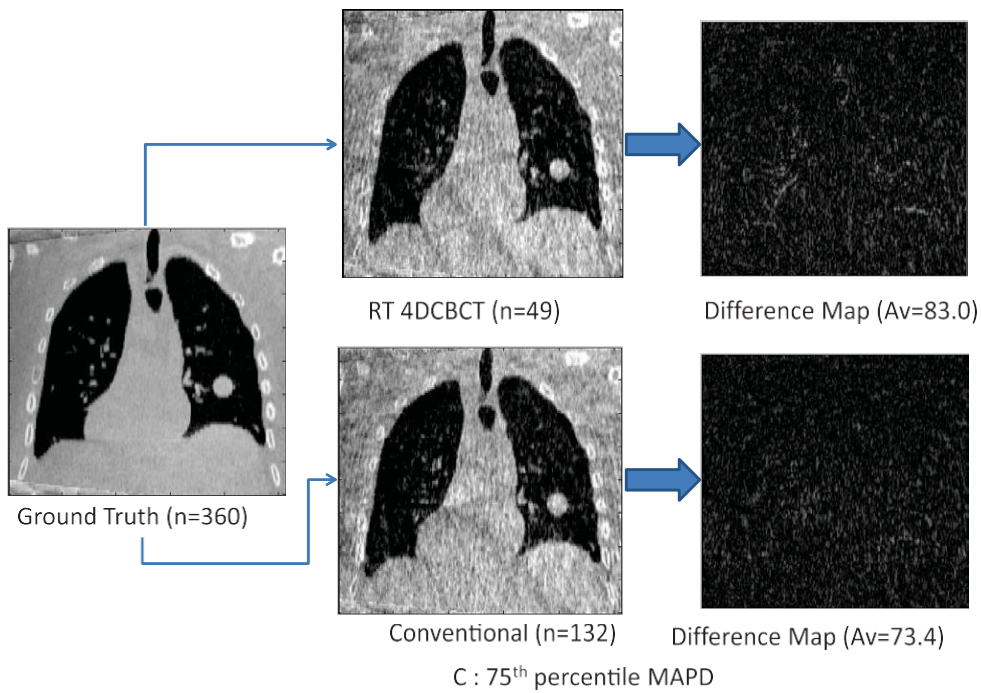Conventional (n=132)   Difference Map (Av=73.4)

C : 75th percentile MAPD

Figure 14. Coronal slices from XCAT simulation corresponding to 75th percentile of *MAPD*. Ground truth image (left), RT 4D CBCT (top) and conventional (bottom), difference maps (right). 'n' is number of projections required, 'Av' is average pixel difference from ground truth image.
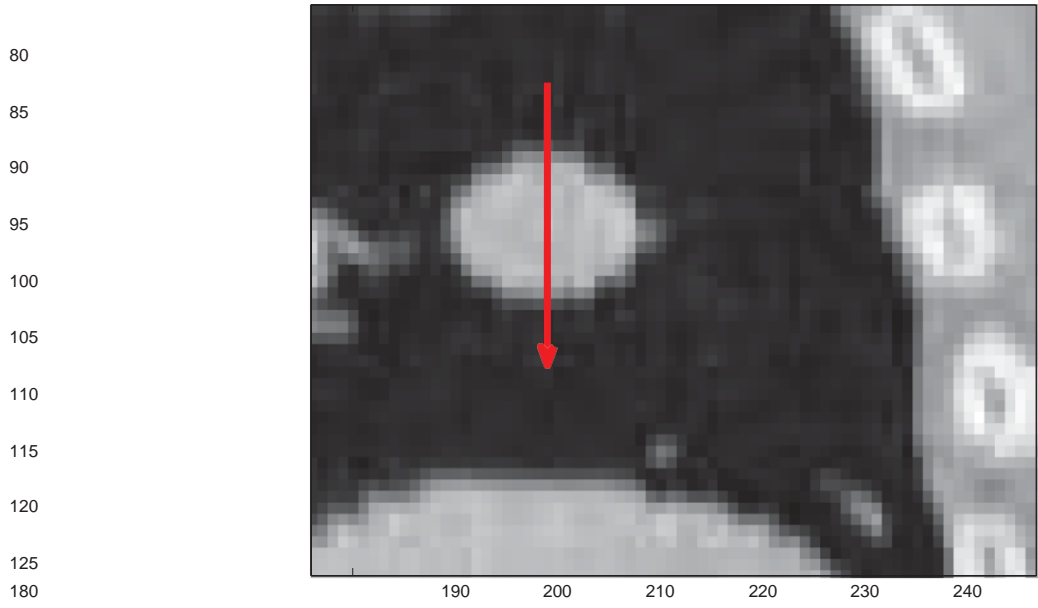
Figure 15. Arrow showing pixel gradient calculation direction (superior to inferior).
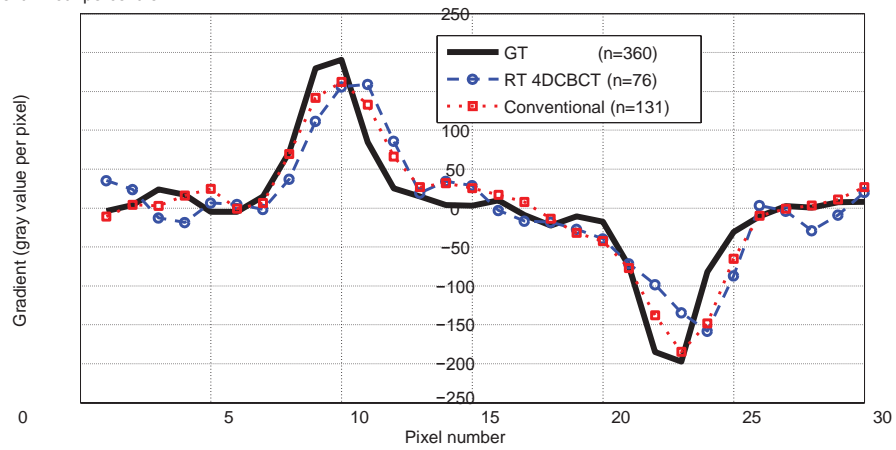
Superior to inferior pixel gradient − 25th percentile

Figure 16. Image gradient calculated in superior to inferior direction for 25th percentile of MAPD simulation. 'n' is the number of projections.

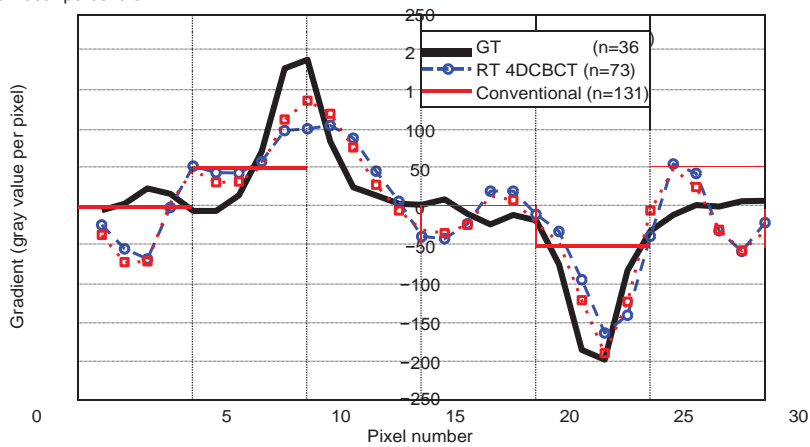Superior to inferior pixel gradient − 50th percentile

Figure 17. Image gradient calculated in superior to inferior direction for 50th percentile of MAPD simulation. 'n' is the number of projections.

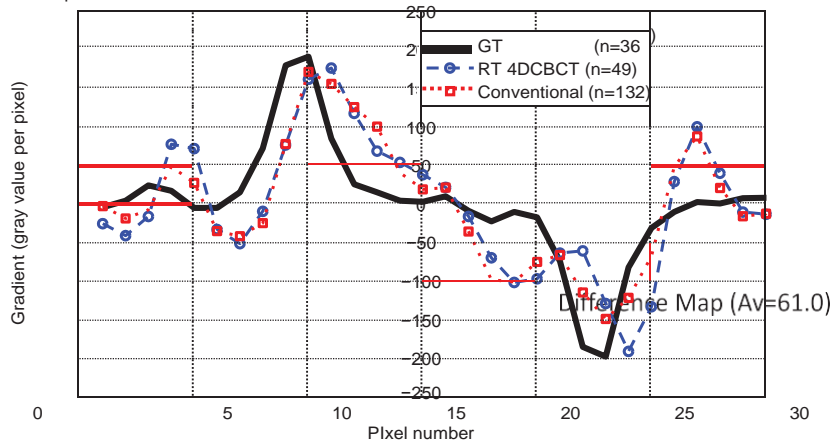Superior to inferior pixel gradient − 75th percentile

Figure 18. Image gradient calculated in superior to inferior direction for 75th percentile of MAPD simulation. 'n' is the number of projections

4   Discussion

It is likely that 4D CBCT will continue to grow as a clinical tool along with an accompanying increase in imaging dose for the patient. It is imperative that any extra imaging dose burden on the patient is utilized in the most efficient way possible. We have demonstrated through simulation studies that the RT 4D CBCT method can offer a substantial saving in imaging dose compared to conventional 4D CBCT. Simulations of RT 4D CBCT and conventional acquisition techniques have been performed for 111 patient-measured breathing traces. Taking the ground truth dataset as a reference, comparisons are presented between the RT 4D CBCT and conventional acquisition methods of the following items:

(i)   Adjacent projection angular spacing distributions;

(ii)   Distributions of *MAPD* from reference ground truth;

(iii)   Distributions of *MAPD* from reference ground truth versus imaging dose;

(iv)   Representative reconstructed images for 25th, 50th, and 75th percentile of *MAPD*.

4.1.   *Adjacent projection angular spacing distribution*

The stand out feature of the two distributions in figure 5 is that the conventional method exhibits an isolated peak in the first histogram bin (≤0.2°) meaning that a large number of adjacent projections are clustered within a respiratory bin and have a small angular separation. This means we have extraneous projections that cost imaging dose but do not add much 'new' anatomical information because the separation is so small. This clustering is a result of the imager triggering at a fixed frequency of roughly 5.5 Hz for the conventional simulations based on Elekta's Symmetry 4D CBCT parameters. In contrast, the RT 4D

CBCT method gives rise to a distribution whose mode is somewhere between 2° and 3° owing to the RT 4D CBCT method triggering once per bin per respiratory cycle. This makes sense as the gantry speed is 0.83 deg. s^{-1} and multiplying this by a population average respiration period of 3.8 s (George *et al* 2005) gives roughly 3° degrees which is similar to the RT 4D CBCT modal angular separation of 2–3°. The other noteworthy feature is the difference in the average number of projections over the 111 breathing traces between conventional (1320) and RT 4D CBCT (617) with the RT 4D CBCT average being about 53% lower than the conventional.

42   *Mean absolute pixel difference from reference ground truth, imaging dose and reconstruction images*

Quantitatively, for the 111 breathing traces used in the Rando studies, the RT 4D CBCT method's average *MAPD* value of 119.2 raw pixel value units is worse than the conventional method's average value of 110.8 raw pixel value units (figure 6); however, qualitatively there is not much difference. Similarly for the XCAT studies the average *MAPD* values are 65.1 and 58.6 for the RT 4D CBCT and conventional methods respectively (figure 7). Representative images from the 25th, 50th and 75th percentiles of *MAPD* from figure 6 are shown in figure 11 and there is little difference between the image progression in the top row (RT 4D CBCT) and the bottom row (conventional). If we now consider the imaging dose for both RT 4D CBCT and conventional simulations there is a stark difference in behaviour. Irrespective of an individual's breathing period, the conventional method will always use about 1320 projections. Figure 8 demonstrates the fixed nature of the conventional method and a sub-optimal use of imaging dose. For the Rando studies, the interquartile range of *MAPD* is 34.55 (89.36–123.91) and for the XCAT studies, the interquartile range is 15.73 (47.83–63.56) but always for a fixed imaging dose. In contrast, for the Rando studies the RT 4D CBCT method gives an interquartile range of *MAPD* of 32.36 (97.85–130.21) and a corresponding spread in dose (486.25–761.25). For the XCAT studies we have an interquartile range of *MAPD* of 19.94 (52.28–72.22) and dose spread of (492.5–770.0). The *MAPD* metric provides a single distilled figure of image difference. One of the limitations of this metric is that it does not give detailed information about the nature of the differences between two images. In this work, both image noise and streaking artifacts contribute to a higher (worse) *MAPD* value; however, the reconstructed images suggest that the streaking artifacts could be the dominant factor in determining the *MAPD*. Suppose we can choose an *MAPD* value of 100. Referring to figure 8 we see that the RT 4D CBCT method requires slightly less than 800 units of imaging dose whereas the conventional method is a flat rate of 1320, representing roughly a 40% saving in imaging dose for the same *MAPD* value. The reason this occurs is because for slower breathers in a fixed 240 s acquisition, there will be fewer breathing cycles compared to a faster breather. Using the RT 4D CBCT method, there is only one projection per bin per breathing cycle and so slower breathers will have fewer projections and thus use less dose compared to a faster breather. In its current form, the RT 4D CBCT algorithm is 'tied' to the respiratory rate of the patient and so slow breathers will always result in fewer projections (and worse images) for a given fixed acquisition time (240 s), in these studies. It is remarkable that the RT 4D CBCT yields a comparable image quality metric (*MAPD*) to conventional 4D CBCT for the very slow breathing outliers (open circles between about 200 and 300 projections in figure 8). This is a 'worst case' for conventional 4D CBCT as it will still use 1320 projections for slow breathers but results in images of similar quality to RT 4D CBCT using 200 to 300

projections. To overcome this problem for slow breathers, an extension to the RT 4D CBCT algorithm could incorporate two projections per phase bin per breath: one at the beginning and one at the end of a phase bin. The goal of such an approach would be to strive for as wide an angular separation as possible within a given phase bin. This would certainly increase projections, but we would see the return to a more 'bunched' pattern of projection acquisitions, although not as bad as conventional 4D CBCT bunching (figure 1). The implication is that if one would like to control the image quality using RT 4D CBCT, then both the gantry velocity and the imaging frequency should be 'tuned' to the respiration rate of the patient, a similar finding to other investigators (Lu *et al* 2007, Ahmad and Pan 2012, Fast *et al* 2013, O'Brien *et al* 2013, 2014).

4.3   *Tumour motion in XCAT studies*

The XCAT studies have shown that the RT 4D CBCT method can produce reconstructed images of a moving target that are of comparable quality to conventional 4D CBCT but with fewer projections. Figures 12–14 illustrate no remarkable qualitative or quantitative difference comparing the RT 4D CBCT and conventional 4D CBCT reconstructed images. There are some discernible patterns of brightness in the difference maps about the liver / lung boundary boundaries. The overall noise and graininess is worst for the 75th percentile (figure 14). The crucial feature to note is that conventional 4D CBCT reconstruction effectively 'wastes' projections (and thus dose) because of the 'bunched' projection pattern that forms (see figure 1(B)). Mauer *et al* have described a step-and-shoot approach whereby fixed stationary gantry positions are chosen and a set of projections are acquired over at least one respiratory period, potentially removing the bunched projection problem; however, this does increase the acquisition time by a few minutes (Maurer *et al* 2010). Similarly to the Rando phantom experiments, the number of projections for a given phase bin (n) used for the RT 4D CBCT simulations is directly proportional to the rate of respiration in the patient ($n = 49$–76), unlike conventional 4D CBCT which uses roughly the same number of projections regardless of the patient's respiration rate ($n = 131$–132) (figures 12–14). Referring to figures 16–18, the ground truth image gradient plot (solid line) compared to both the RT 4D CBCT and conventional plots follow the same general shape; however the maxima and minima are quite variable and the '0' gradient regions become noisier going from figures 12–14 for both RT 4D CBCT and conventional simulations. The gradient data is taken to represent tumour detectability by eye. The plots in figures 16–18 suggest that there is little difference between the RT 4D CBCT and conventional lesion detectability although there is evidence of a minor positional shift in both the RT 4D CBCT and conventional plots. The maxima and minima appear to be shifted by roughly 1 pixel (1.2 mm is the CBCT slice thickness in the *z*-direction) in the superior- inferior direction suggesting a lag between the where the tumour actually is (according to the ground truth gradient plot) and the detected tumour location (RT 4D CBCT and conventional plots). The positional error in tumour location detection in these studies implies a targeting accuracy no better than 1.2 mm. There is a substantially higher cost in dose to achieve this level of accuracy (number of projections 'n') for conventional 4D CBCT compared to RT4D CBCT.

# 5	Conclusion

The simulation studies have demonstrated that the RT 4D CBCT method can potentially offer a substantial saving of imaging dose in the order of about 53% on average compared to conventional 4D CBCT using a wide range of patient breathing traces with a minimal impact on image quality.

References

Abdelnour A *et al* 2007 Phase and amplitude binning for 4D-CT imaging *Phys. Med. Biol.* **52** 3515

Ahmad M and Pan T 2012 Target-specific optimization of four-dimensional cone beam computed tomography *Med. Phys.* **39** 5683–96

Brehm M, Berkus T, Oehlhafen M, Kunz P and Kachelriess M 2011 Motion-compensated 4D cone- beam computed tomography *Nuclear Science Symp. and Medical Imaging Conf.* pp 3986–93

Brehm M, Paysan P, Oelhafen M and Kachelrieß M 2013 Artifact-resistant motion estimation with a patient-specific artifact model for motion-compensated cone-beam CT *Med. Phys.* **40** 101913

Cooper B J, O'Brien R T, Balik S, Hugo G D and Keall P J 2013 Respiratory triggered 4D cone-beam computed tomography: a novel method to reduce imaging dose *Med. Phys.* **40** 41901

Fast M F, Wisotzky E, Oelfke U and Nill S 2013 Actively triggered 4d cone-beam CT acquisition *Med. Phys.* **40** 91909

Feldkamp L A, Davis L C and Kress J W 1984 Practical cone-beam algorithm *J. Opt. Soc. Am.* A **1** 612–9

George R, Chung T D, Vedam S S, Ramakrishnan V, Mohan R, Weiss E and Keall P J 2006 Audio- visual biofeedback for respiratory-gated radiotherapy: impact of audio instruction and audio-visual biofeedback on respiratory-gated radiotherapy *Int. J. Radiat. Oncol. Biol. Phys.* **65** 924–33

George R, Vedam S S, Chung T D, Ramakrishnan V and Keall P J 2005 The application of the sinusoidal model to lung cancer patient respiratory motion *Med. Phys.* **32** 2850

Giaddui T, Cui Y, Galvin J, Yu Y and Xiao Y 2013 Comparative dose evaluations between XVI and OBI cone beam CT systems using Gafchromic XRQA2 film and nanoDot optical stimulated luminescence dosimeters *Med. Phys.* **40** 62102

Ionascu D, Jiang S B, Nishioka S, Shirato H and Berbeco R I 2007 Internal-external correlation investigations of respiratory induced motion of lung tumors *Med. Phys.* **34** 3893–903

Jia X, Dong B, Lou Y and Jiang S B 2011 GPU-based iterative cone-beam CT reconstruction using tight frame regularization *Phys. Med. Biol.* **56** 3787–807

Jia X, Lou Y, Li R, Song W Y and Jiang S B 2010 GPU-based fast cone beam CT reconstruction from undersampled and noisy projection data via total variation *Med. Phys.* **37** 1757–60

Keall P J *et al* 2006 The management of respiratory motion in radiation oncology report of AAPM Task Group 76a *Med. Phys.* **33** 3874–900

Kim S, Yoo S, Yin F F, Samei E and Yoshizumi T 2010 Kilovoltage cone-beam CT: comparative dose and image quality evaluations in partial and full-angle scan protocols *Med. Phys.* **37** 3648

Kincaid R E Jr, Yorke E D, Goodman K A, Rimner A, Wu A J and Mageras G S 2013 Investigation of gated cone-beam CT to reduce respiratory motion blurring *Med. Phys.* **40** 41717

Leng S, Tang J, Zambelli J, Nett B, Tolakanahalli R and Chen G H 2008a High temporal resolution and streak-free four-dimensional cone-beam computed tomography *Phys. Med. Biol.* **53** 5653

Leng S, Zambelli J, Tolakanahalli R, Nett B, Munro P, Star-Lack J, Paliwal B and Chen G H 2008b Streaking artifacts reduction in four-dimensional cone-beam computed tomography *Med. Phys.* **35** 4649–59

Li T and Xing L 2007 Optimizing 4D cone-beam CT acquisition protocol for external beam radiotherapy *Int. J. Radiat. Oncol. Biol. Phys.* **67** 1211–9

Lu J, Guerrero T M, Munro P, Jeung A, Chi P C M, Balter P, Zhu X R, Mohan R and Pan T 2007 Four-dimensional cone beam CT with adaptive gantry rotation and adaptive data sampling *Med. Phys.* **34** 3520

Maurer J, Pan T and Yin F F 2010 Slow gantry rotation acquisition technique for on-board four-dimensional digital tomosynthesis *Med. Phys.* **37** 921–33

O'Brien R T, Cooper B J and Keall P J 2013 Optimizing 4D cone beam computed tomography acquisition by varying the gantry velocity and projection time interval *Phys. Med. Biol.* **58** 1705

O'Brien R T, Cooper B J, Kipritidis J, Shieh C C and Keall P J 2014 Respiratory motion guided four dimensional cone beam computed tomography: encompassing irregular breathing *Phys. Med. Biol.* **59** 579

Qi Z and Chen G H 2011 Extraction of tumor motion trajectories using PICCS-4DCBCT: a validation study *Med. Phys.* **38** 5530

Rit S, Sarrut D and Desbat L 2009 Comparison of analytic and algebraic methods for motion-compensated cone-beam CT reconstruction of the thorax *IEEE Trans. Med. Imaging* **28** 1513–25

Rit S, Oliva M V, Brousmiche S, Labarbe R, Sarrut D and Sharp G C 2014 The reconstruction toolkit (RTK), an open-source cone-beam CT reconstruction toolkit based on the insight toolkit (ITK)

J. Phys.: Conf. Ser. **489** 2079

Rosu M and Hugo G D 2012 Advances in 4D radiation therapy for managing respiration: part II–4D treatment planning *Z. Med. Phys*. **22** 272–80

Ruan D, Fessler J A, Balter J and Keall P 2009 Real-time profiling of respiratory motion: baseline drift, frequency variation and fundamental pattern change *Phys. Med. Biol.* **54** 4777

Santoro J P, Yorke E, Goodman K A and Mageras G S 2009 From phase-based to displacement-based gating: a software tool to facilitate respiration-gated radiation treatment *J. Appl. Clin. Med. Phys.* **10** 2982

Segars W P, Sturgeon G, Mendonca S, Grimes J and Tsui B M W 2010 4D XCAT phantom for multimodality imaging research *Med. Phys.* **37** 4902–15

Shrimpton P, Wall B and Fisher E 1981 The tissue-equivalence of the Alderson Rando anthropomorphic phantom for x-rays of diagnostic qualities *Phys. Med. Biol.* **26** 133

Sonke J J, Lebesque J and van Herk M 2008 Variability of four-dimensional computed tomography patient models *Int. J. Radiat. Oncol. Biol. Phys.* **70** 590–8

Sweeney R, Seubert B, Stark S, Homann V, Muller G, Flentje M and Guckenberger M 2012 Accuracy and inter-observer variability of 3D versus 4D cone-beam CT based image-guidance in SBRT for lung tumors *Radiat. Oncol.* **7** 81

Takahashi W, Yamashita H, Kida S, Masutani Y, Sakumi A, Ohtomo K, Nakagawa K and Haga A 2013 Verification of planning target volume settings in volumetric modulated arc therapy for stereotactic body radiation therapy by using in-treatment 4-dimensional cone beam computed tomography *Int. J. Radiat. Oncol. Biol. Phys*. **86** 426–31

Wang J and Gu X 2013 High-quality four-dimensional cone-beam CT by deforming prior images *Phys. Med. Biol.* **58** 231

Zhang Y, Yin F F, Segars W P and Ren L 2013 A technique for estimating 4D-CBCT using prior knowledge and limited-angle projections *Med. Phys.* **40** 121701